Energy & Environmental Science

Volume 11
Number 4
April 2018
Pages 719-1000

rsc.li/ees

ISSN 1754-5706

ROYAL SOCIETY OF CHEMISTRY

REVIEW ARTICLE
Yuekun Lai, Zhiqun Lin et al.
Graphene aerogels for efficient energy storage and conversion

ROYAL SOCIETY OF CHEMISTRY

rsc.li/ees

Broader Context:

Long-term stability is a critical problem towards the commercialization of perovskite solar cells (PSCs). Herein, we propose an *in-situ* cross-linked polymer (**Spiro-NPU**) as an internal encapsulating layer (IEL) with a strong hydrophobicity. With this strategy, **Spiro-NPU** IEL not only protects perovskite films from moisture, heat and defect induced degradation, realizing a long-term device stability, but also blocks the lead-leakage from environmental contamination. Furthermore, **Spiro-NPU** endows a promising self-repairability of PSCs, as an ingenious strategy to elongate the device lifetime. Therefore, we ensure that internal encapsulation could be an effective and promising way to finally solve the stability problem of perovskite solar cells and realize efficient, stable, repairable and low-lead-leakage PSCs.

ARTICLE

An Internal Encapsulating Layer for Efficient, Stable, Repairable and Low-lead-leakage Perovskite Solar Cells

Dongdong Xu, [a] Runsheng Mai, [a] Yue Jiang, *[a] Cong Chen, [a,b] Ru Wang, [a] Zhengjie Xu, [a] Krzysztof Kempa, [c] Guofu Zhou, [d] Jun-Ming Liu,[a, e] Jinwei Gao *[a]

Perovskite solar cells (PSCs) have achieved remarkable progress with high power conversion efficiency (PCE) and low cost. However, there is still huge room for improvement in terms of long-term stability, repairability and lead toxicity reduction, before its large-scale industrialization can start. Here, we propose an internal encapsulating layer (IEL) based on an *in-situ* cross-linked insoluble polymer (**Spiro-NPU**), with matched energy levels, good electrical conductivity and matched hole mobility. While the insertion of **Spiro-NPU** significantly enhanced the photovoltaic performance, with champion PCEs reaching 23.26% on rigid substrates and about 20% for flexible devices, most importantly the IEL strongly enhances the moisture/thermal stability, as well as the repairability of the PSCs. No PCE decay have been observed after 3000 h of aging in air, at 60% relative humidity (RH); over 90% of initial efficiency was maintained after 500 h of aging at 85% RH @ 25°C (or at 55% RH @ 85°C); even 97% of their initial PCE was retained after operating at the maximum power point (MMP) under 1 sun illumination (~50°C in N$_2$) for 200 hours without any external encapsulations. In addition, the photovoltaic-inactive hydrated phase of the perovskite films after one-month aging (85% RH @ 25°C), recovers back into the photovoltaic-active black phase, after annealing or one solar irradiation, and its corresponding PSCs have also shown this repairability. Furthermore, our IEL exhibits a capability of lead blocking, paving the way for a promising strategy towards stable, efficient and safe PSCs.

Introduction

Organic-inorganic hybrid perovskite solar cells (PSCs), as one of the most promising technologies towards the renewable and clean energy, have achieved the power conversion efficiency exceeding 25%,[1] *i.e.* matching with this respect to the Si- based solar cells. The monolithic perovskite/silicon tandem solar cells achieved *PCE* close to 30%.[1] However, due to the ionic nature of the perovskite materials, their long-term stability against moisture/heat remains poor, and is still the most important obstacle to commercial applications.[2,3] In addition, the lead leakage during the usage remains an environmental safety concern.

Several strategies have been investigated to solve the stability problem. External encapsulating layers (EEL) based on hydrophobic polymers to physically block the moisture intrusion is a universal method. For example, Fu *et al.*[4] and Matteo *et al.*[5] successively reported polyurethane (PU) as an EEL which resulting in retaining 97.52% of initial *PCE* after ~2100 h storage at outdoor environment. Other polymeric EELs, such as, epoxy;[6] polyisobutylene (PIB);[7] polyolefin (POE);[8] ethylene vinyl acetate (EVA);[9] and paraffin[10] *etc*, have also been investigated. However, the protection of EELs is rather limited since the internal instabilities, *eg*, lattice defects of the perovskite active layer,[11-13] and the diffusion of ions/molecules[14-17] are also the key factors affecting the stability of the perovskite. Researchers proposed to utilize an internal encapsulating layer (IEL) as a complement of EEL to improve the stability of the perovskite films, which involves the grain boundary encapsulation by polymer doping in perovskite films[18-22]，such as polyethylene glycol (PEG) and polyurethane (PU), and the perovskite/HTL interface encapsulation by polymeric interfacial materials,[23-29] such as poly(methylmethacrylate) (PMMA) and polystyrene (PS). Whereas the quantity of dopant or the thickness of interface is quite low. Thus, their long-term protection against the moisture remains inadequate.

Attempts to tackle the lead leakage have been focusing on the interface engineering. For instance, Wu *et al*. have introduced a metal–organic frameworks (MOFs) ZrL3 to capture the Pb^{2+} leaked from the degraded films.[30] Chen *et al* doped a mesoporous sulfonic acid-based resin in perovskite to fix in place the lead ions.[31] In addition, EELs based on phosphonic acid,[32] epoxy groups[33] and cation-exchange resin[34] were proved to effectively reduce lead leakage as well.

In our work, we have adopted a layer of IEL to simultaneously maintain the efficiency and enhance the

[a.] *Institute for Advanced Materials and Guangdong Provincial Key Laboratory of Optical Information Materials and Technology, South China Academy of Advanced Optoelectronics, South China Normal University, Guangzhou 510006, China.*

[b.] *Department of Mechanical Engineering, The University of Hong Kong, Pokfulam Rd., Pokfulam, Hong Kong.*

[c.] *Department of Physics, Boston College, Chestnut Hill, Massachusetts 02467, USA.*

[d.] *Guangdong Provincial Key Laboratory of Optical Information Materials and Technology & Institute of Electronic Paper Displays, South China Academy of Advanced Optoelectronics, South China Normal University, Guangzhou 510006, China.*

[e.] *Laboratory of Solid-State Microstructures, Nanjing University, Nanjing 210093, China.*

Electronic Supplementary Information (ESI) available: [details of any supplementary information available should be included here]. See DOI: 10.1039/x0xx00000x

stability and lead blocking capability. Due to the better diffusion of small molecules than high molecular weight polymers[35] and the obtained higher morphology reproducibility[36] with in-situ polymerization, and the stronger capability in blocking moisture ingestion of cross-linked polymers,[37] the in-situ cross-linked thick polymers are highly desired. We aimed to modify high-performing Spiro-OMeTAD HTMs for cross-linking to enable improved diffusion barrier properties with minimal effects on the electronic and chemical properties. Our designed and synthesized *in-situ* co-polymerized IEL (**Spiro-NPU**)，based on 2,2',2'',2'''-(((9,9'-spirobi[fluorene]-2,2',7,7' tetrayltetrakis(phe-nylazanediyl))tet-rakis(ethane-2,1-diyl))tetr-akis(oxy))tetrakis(-etan-1-ol) (**Spiro-OH**), and 1,5-naphthalene diisocyanate (**NDI**) monomers, enhances the moisture resistance and lead blockage by virtue of the spiro block, NCO and carbonyl groups.

Results and Discussion

### Synthesis and characterization

The target internal encapsulating material, cross-linked **Spiro-NPU** polymer, was obtained according to the synthetic route as illustrated in **Fig. 1a** and **Fig. S1**. The mixed **Spiro-OH** and **NDI** solution in chlorobenzene (CB) was firstly pre-polymerized at 85°C for 6 hours, followed by the hot spin-coating on top of the perovskite films. The as-obtained **Spiro-NPU** films were used without further purification.

From the Fourier-transform infrared (FTIR) spectra (**Fig. 1b**), **Spiro-NPU** polymer shows the characteristic peaks of urethane group at 3336 cm^{-1} and 1718 cm^{-1}, corresponding to

with the FTIR spectra of **Spiro–OH** and **NDI**. This is further confirmed by checking their ^{1}H nuclear magnetic resonance (NMR) spectra (**Fig. S2**), where the characteristic chemical shift of -OH (4.52 - 4.50 ppm) disappeares along with the appearance of urethane group at downfield (10 - 9 ppm) for **Spiro-NPU**. However, due to the poor solubility of **Spiro-NPU**, its molecular weight can not be obtained, we then measure the corresponding molecular weight of the pre-polymer as shown in **Fig. S3**. In addition, the melting point of Spiro-NPU is absent from Differential Scanning Calorimetry (DSC, in **Fig. S4**), we considered that the crosslinking degree of our **Spiro-NPU** is relatively high.

The optical and electrochemical properties of the **Spiro-NPU** film were examined by UV-vis absorption spectrometer and ultraviolet photoelectron spectroscopy (UPS), where the optical bandgap (E_g) and the highest occupied molecular orbital (HOMO) energetic level were determined to be 3.21 eV and -5.29 eV (**Fig. S5-S7**). These results were also confirmed by the cyclic voltammetry (CV) as illustrated in **Fig. S8**. Compared with the energetic structures of perovskite materials, *eg*, $CH_3NH_3PbI_3$ and $Cs_{0.05}FA_{0.85}MA_{0.10}Pb(Br_{0.03}I_{0.97})_3$, **Spiro-NPU** matches well than others and thus enables effectively the transfer of holes and the blocking of back-transfer electrons (**Fig. S9, Table S1**).

Subsequently, the morphology of **Spiro-NPU** IEL on top of perovskite film was studied by scanning electron microscope (SEM). From **Fig. 1c**, the uniform and compact perovskite film was covered with a smooth and flat surface of **Spiro-NPU**. We have further confirmed the morphology of **Spiro-NPU** by AFM,
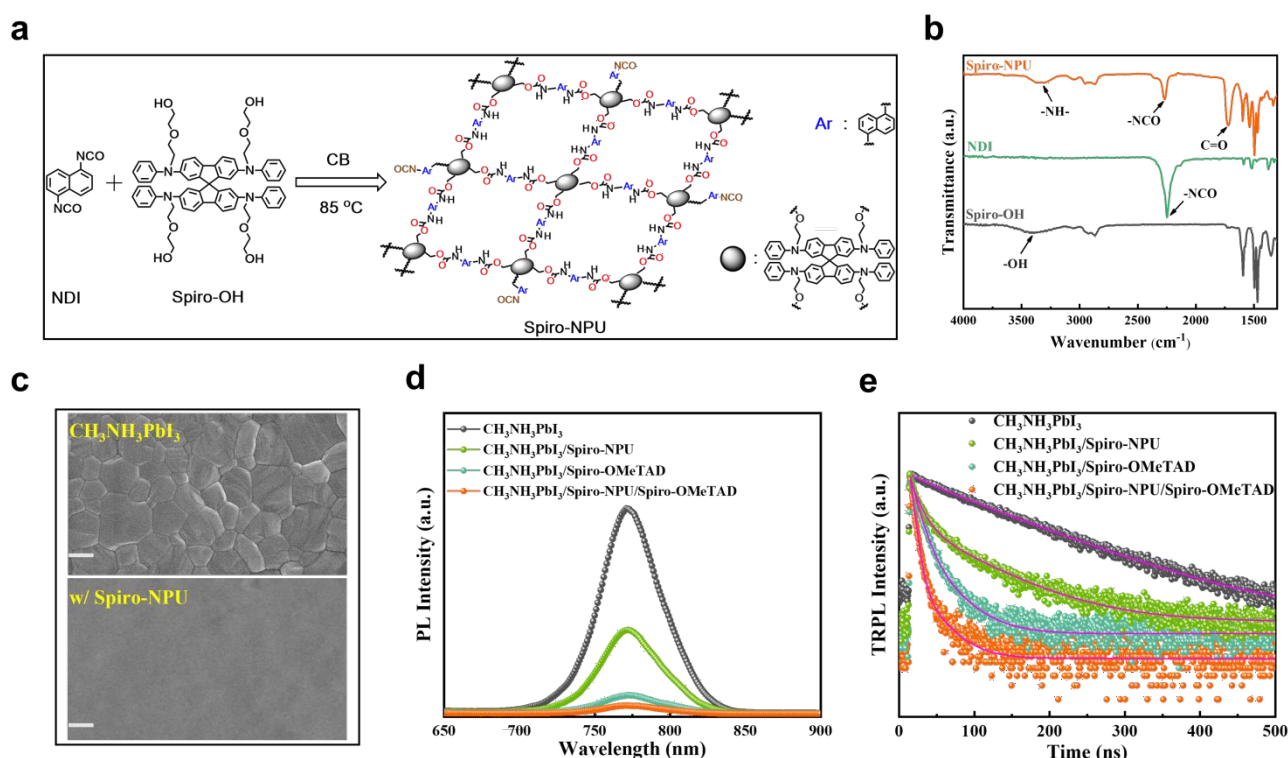
the stretching vibrations of N–H and C=O groups, respectively.[18] **Spiro-NPU** was found terminated with NCO groups, because only NCO group at 2266 cm^{-1} was observed without the stretching vibration of O-H bond at ~3446 cm^{-1} when comparing

showing a low root-mean-square (RMS) of 5.83 nm (**Fig. S10**).

Fig. 1. **Synthesis and characterization of Spiro-NPU IEL. (a**) Synthetic route of the cross-linked **Spiro-NPU** IEL. (**b**) FTIR spectra of **Spiro-OH**, **NDI** and **Spiro-NPU**. (**c**) Top-view SEM images of $CH_3NH_3PbI_3$ and $CH_3NH_3PbI_3$/**Spiro-NPU**. Scale bar: 500 nm. (**d**) Steady-state PL. (**e**) TRPL spectra of the glass/$CH_3NH_3PbI_3$, glass/$CH_3NH_3PbI_3$/**Spiro-NPU**, glass/$CH_3NH_3PbI_3$/Spiro-OMeTAD, and glass/$CH_3NH_3PbI_3$/**Spiro-NPU/**Spiro-OMeTAD.

To elucidate the charge extraction and transportation capability of **Spiro-NPU** IEL on account of its position between perovskite and hole transport material, steady-state photoluminescence (PL) and space charge limited current (SCLC) were conducted. As shown in **Fig. 1d**, the luminescence of the perovskite with **Spiro-NPU** was significantly quenched compared to that of pristine film, suggesting the decent hole extraction efficiency of **Spiro-NPU**. While the calculated hole mobility for the device ITO/PEDOT:PSS/**Spiro-NPU**/Spiro-OMeTAD/Ag was 6.53×10^{-3} cm^2/Vs, with the same order of

parameters are summarized in **Table S2**. Generally, $\tau 1$ represents the charge transfer from perovskite to Spiro-OMeTAD, which relates to the non-radiative recombination caused by surface defects, while $\tau 2$ represents the radiative recombination process caused by the traps in the perovskite layer.[39-41] Thereby, the observed shorter τ_{ave}, *ca.* 10.19 ns, indicates a quick photogenerated carriers transfer process from perovskite to Spiro-OMeTAD when **Spiro-NPU** was inserted.
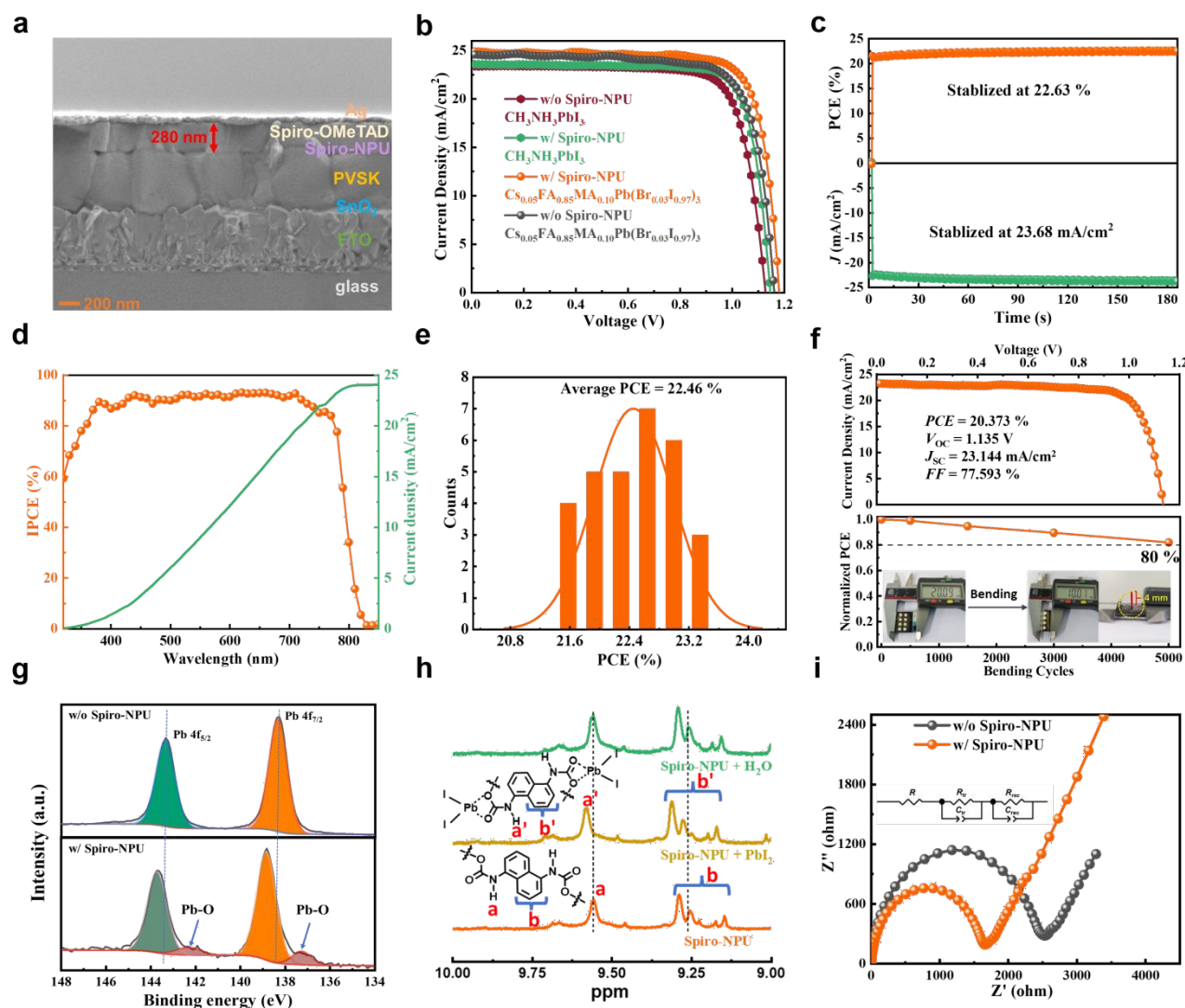

Fig. 2. PSCs Performances. (**a**) Cross-sectional SEM image of $CH_3NH_3PbI_3$-PSC with **Spiro-NPU**. (**b**) *J–V* curves of the champion devices based on $CH_3NH_3PbI_3$ and $Cs_{0.05}FA_{0.85}MA_{0.10}Pb(Br_{0.03}I_{0.97})_3$ absorbers, respectively. (**c**) The steady-state *PCE* and photocurrent measurements at maximum power point of the device with **Spiro-NPU**. (**d**) EQE spectra and integrated photocurrent curves of the device with **Spiro-NPU**. (**e**) *PCE* histogram obtained from 30 PSCs with **Spiro-NPU** IEL. (**f**) *J–V* curves and the normalized *PCE* as a function of bending cycles of flexible devices. (**g**) XPS spectra. (**h**) ^{1}H NMR spectra of **Spiro-NPU** with or without PbI_2. The NMR reference chemical shift is the tetramethylsilane (TMS). (**i**) Nyquist plots of PSCs under the dark condition at 0.7 V bias. **The devices of c, d, e, f, g, and i have the same active layer of $Cs_{0.05}FA_{0.85}MA_{0.10}Pb(Br_{0.03}I_{0.97})_3$.**

magnitude of the device without **Spiro-NPU** (1.08×10^{-3} cm^2/Vs) (**Fig. S11**).[38]
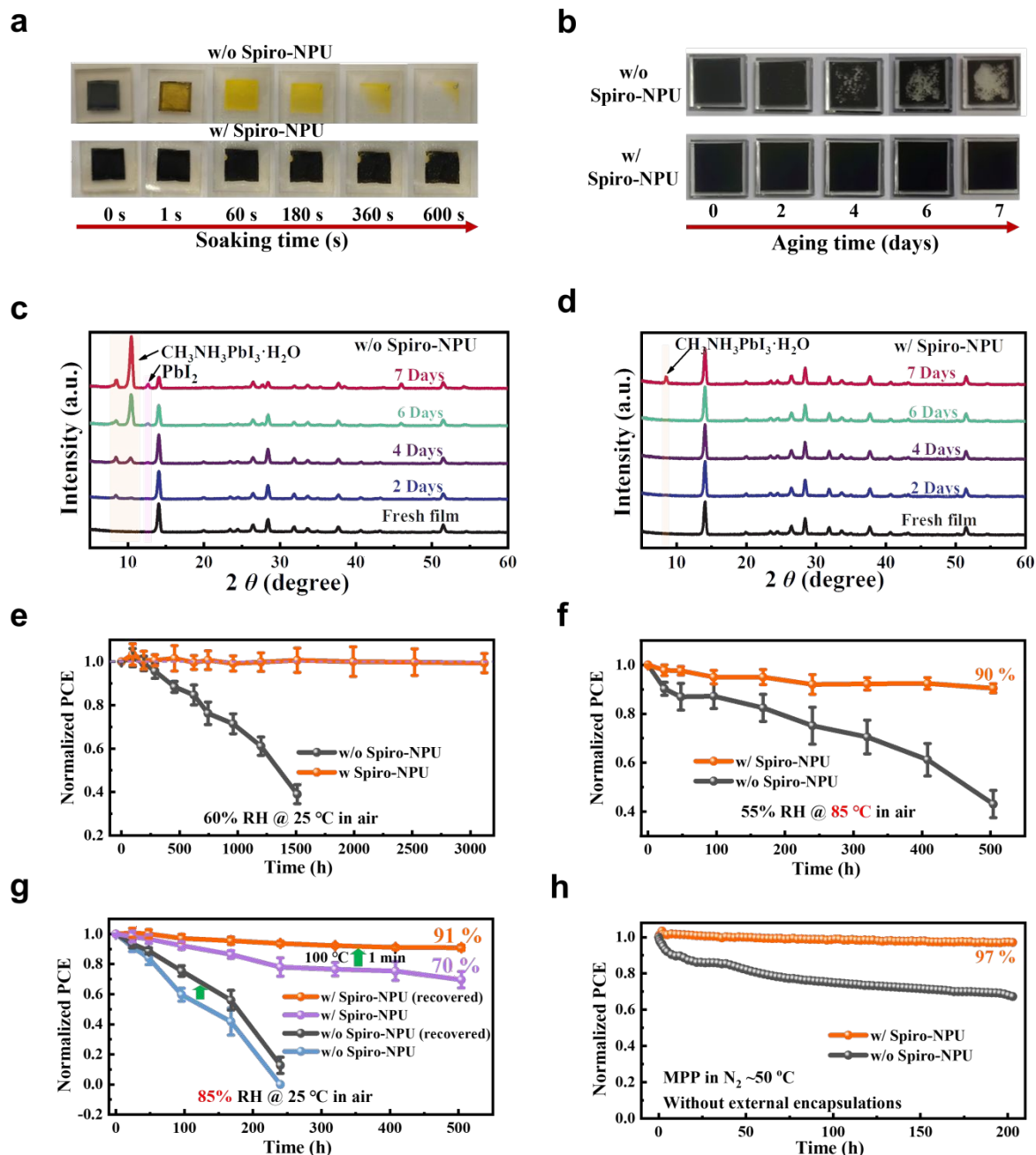
Fig. 1e displays the time-resolved photoluminescence (TRPL) decay curves, which could be fitted by bi-exponential decay function: $f(t) = A1exp(-t/\tau 1) + A2exp(-t/\tau 2)$, where A1 and A2 are the decay amplitudes and τ is the decay time. The fitted

Photovoltaic performance of rigid and flexible devices

ARTICLE

Based on these desirable properties of **Spiro-NPU**, we have fabricated the n-i-p type planar PSCs with structure configuration of FTO/SnO₂/CH₃NH₃PbI₃/**Spiro-NPU**/Spiro-OMeTAD/Ag, as shown in the cross-sectional SEM image (**Fig. 2a**). The thickness of **Spiro-NPU** is about 115 nm, which was optimized based on the output of 20 independent PSCs fabricated with different concentration of **Spiro-NPU** (**Fig. S12, S13, Table S3**). From the current density-voltage (J-V) curves in **Fig. 2b**, the champion PCE of 21.69% was achieved after inserting **Spiro-NPU**, along with the open circuit voltage (V_{OC}) of 1.15 V, short circuit current density (J_{SC}) of 23.58 mA/cm², and fill factor

was utilized as the light absorber as presented in the J-V curves in **Fig. 2b**, which is also obviously better than the **Spiro-NPU**-free device.

This high PCE based on Cs₀.₀₅FA₀.₈₅MA₀.₁₀Pb(Br₀.₀₃I₀.₉₇)₃ was confirmed by monitoring the stabilized output at the maximum power point (MPP) for the **Spiro-NPU** modified device under continuous AM 1.5G illumination. **Fig. 2c** reveals the stabilized PCE of 22.63% with J_{SC} of 23.68 mA/cm² which is in good agreement with the PCE obtained from the J-V curves. The external quantum efficiency (EQE) measurement in **Fig. 2d** also exhibits the nearly

Fig. 3. Stability evaluation of CH₃NH₃PbI₃ modified with Spiro-NPU IEL. (a) Photographs of the CH₃NH₃PbI₃ films without and with **Spiro-NPU** soaking in water. **(b)** Photographs of the CH₃NH₃PbI₃ films with and without **Spiro-NPU** exposed to 85 % RH. **(c-d)** XRD patterns of the CH₃NH₃PbI₃ films without and with **Spiro-NPU**. **(e-g)** The stability of perovskite devices with and without **Spiro-NPU** IEL under various moisture and heat. The error bars represent the standard deviations from ten samples for each condition. **(h)** Maximum power point tracking under full solar illumination (AM 1.5G, 100 mW/cm²) in glovebox.

(FF) of 80.28%. It is clear that the FF and V_{OC} was greatly enhanced when comparing with the **Spiro-NPU**-free control device (PCE = 20.51%, J_{SC} = 23.39 mA/cm², FF = 77.83%, and V_{OC} = 1.13 V) (**Fig. S14**). This PCE was then further increased to 23.26% (J_{SC} = 24.79 mA/cm², FF = 79.49%, and V_{OC} = 1.18 V) when Cs₀.₀₅FA₀.₈₅MA₀.₁₀Pb(Br₀.₀₃I₀.₉₇)₃

equivalent integrated J_{SC} = 24.12 mA/cm² with the obtained J_{SC} from J-V curves. The reproducibility of the device was then verified by fabricating 30 independent devices, achieving an average PCE of 22.46% (**Fig. 2e, Fig. S15**). The statistical distributions are summarized in **Table S4**. The average V_{OC}, J_{SC}, and FF based on **Spiro-**

NPU are 1.17 V, 24.65 mA /cm^2, 78.12% respectively, significantly larger than those of the control devices, especially for V_{OC} and FF.

Moreover, the flexible PSCs were fabricated with the device configuration of PEN/ITO/SnO$_2$/Cs$_{0.05}$FA$_{0.85}$MA$_{0.10}$Pb(Br$_{0.03}$I$_{0.97}$)$_3$/**Spiro-NPU**/Spiro-OMeTAD/Ag. **Fig. 2f** shows the J–V curves of the best device, where the PCE of 20.37% (V_{OC} = 1.14 V, J_{SC} = 23.11 mA/cm^2, FF = 77.59%) was achieved. By tracking the PCE during the repeated bending test over 5000 times under a lower curvature radius (about 4 mm), device with **Spiro-NPU** maintained over 80% of the original efficiency. This is highly related to the release of mechanical stress by the thick **Spiro-NPU** IEL due to the formation of tight contacting during the *in-situ* synthesis, as suggested by the observation of a conspicuous peak corresponding to the Pb-O bond [42,43] between acylamino groups and Pb^{2+}, at 137.2 eV and 142.2 eV, in the X-ray photoelectron spectroscopy (XPS) in **Fig. 2g**.

The mechanism of the enhanced performance was then investigated. Except the XPS characterization (**Fig. 2g**), the strong interaction between the acylamino groups and Pb^{2+} was demonstrated by ^{1}H NMR in **Fig. 2h**, **Fig. S16,** where the peaks of the H^a and H^b slightly downfield shifted when PbI$_2$ was added into the **Spiro-NPU** solution,[44] and the water was added directly to **Spiro-NPU** solution to eliminate the influence of H$_2$O on NMR chemical shift. Together with the calculated hole-trap density, *ca* 6.53 × 10^{15} cm^{-3} vs 9.45 × 10^{15} cm^{-3} for devices with and without **Spiro-NPU** via SCLC measurement (**Fig. S17a**),[45] respectively, the effective trap passivation of **Spiro-NPU** at the perovskite surface was validated.

Further, the trap related recombination was analyzed by comparing the V_{OC} dependence on light intensity, where the ideality factor (n_{id}) represents the device diode characteristic correlating to the non-radiative recombination.[46] **Fig. S17b** exhibits a smaller n_{id} (1.65) for **Spiro-NPU** modified device than that of the control device (2.63), interpretive of the reduced recombination and so as to the enhanced V_{OC} and FF.[22, 47]

In the meantime, the electrochemical impedance spectroscopy (EIS) measurements and dark J–V measurements were conducted to evaluate the charge transport and recombination processes in the device. From Nyquist plot presented in **Fig. 2i**, the semicircles at high frequency and at low frequency are generally assigned to the charge transfer and recombination processes, corresponding to resistance of R_{tr} and R_{rec}, respectively.[48,49] Thereby, the both shrunk semicircles of device with **Spiro-NPU** are indicative of the facilitated charge transport with mitigated recombination. In addition, from the lower (2.98 × 10^{-8} mA/cm^2) leakage current (J_0) for the **Spiro-NPU** modified device than that of the control device (1.77 × 10^{-7} mA cm^{-2}) at both negative and positive bias voltage (**Fig. S17c**), the same conclusion could be deduced that the addition of **Spiro-NPU** can prominently improve the hole transfer efficiency and decrease recombination loss.[50]

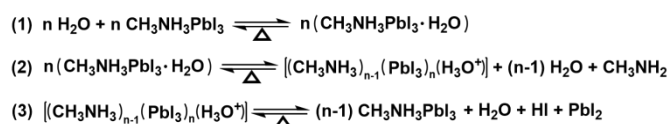## Stability and repairability of CH$_3$NH$_3$PbI$_3$

Since CH$_3$NH$_3$PbI$_3$ is most used light absorber and also more sensitive to humidity, it is adopted in order to demonstrate the encapsulating capability of our IELs. As an internal encapsulating material, the influence of **Spiro-NPU** on the

moisture and thermal stability is of fundamental importance. By comparing with the pristine CH$_3$NH$_3$PbI$_3$ film, the water contact angle of perovskite/**Spiro-NPU** is obviously larger (110° vs 52.6°) (**Fig. S18**). When directly immersing the perovskite films into deionized water, as shown in **Fig. 3a** and **Video S1** (Supplementary), the bare film decomposed into yellow PbI$_2$ at the moment of contacting, followed by quickly dissolve and lead contamination.[32] In sharp contrast to that, the perovskite film protected with **Spiro-NPU** IEL shows amazing water resistance over 15 min.

Furthermore, we have tracked the optical and crystalline properties of the perovskite films during decomposing at 85% RH in one week (**Fig. 3b**). The perovskite films covered with **Spiro-NPU** IEL maintained its black phase during the whole week, whereas the pristine perovskite deteriorated from black phase to transparent hydrated phase and yellow PbI$_2$. This is confirmed by XRD, that an obvious hydrated derivative peak (2ϑ = 10.6°, 8.5°) accompanied by PbI$_2$ (2ϑ = 12.6°)[51] was observed for pristine perovskite film, while with **Spiro-NPU** IEL, only a weak monohydrate peak (2ϑ = 8. 5°) was observed (**Fig. 3c**).[52]

By extending the aging time to one month at 85% RH, completely transparent hydrated perovskite films were obtained. However, after heating (100°C, 1 min) or one solar irradiation (8 min), this hydrated **Spiro-NPU** IEL protected perovskite film was surprisingly turned back into black mirror morphology, showing a vital repairability, which helps to extend the overall lifetime of PSCs. This phenomenon is mainly due to the fact that with **Spiro-NPU** IEL, only CH$_3$NH$_3$PbI$_3$·H$_2$O[53, 54] was formed without further decomposing into PbI$_2$, as illustrated by XRD in **Fig. S19, S20**.

As reported in the literature,[51, 53] the decomposition of CH$_3$NH$_3$PbI$_3$ catalyzed by water follows the reversible reaction equations (1), (2) & (3) as shown below:

$$(1)\ \ n\,H_2O + n\,CH_3NH_3PbI_3 \underset{\Delta}{\rightleftharpoons} n(CH_3NH_3PbI_3 \cdot H_2O)$$

$$(2)\ \ n(CH_3NH_3PbI_3 \cdot H_2O) \underset{\Delta}{\rightleftharpoons} \left[(CH_3NH_3)_{n-1}(PbI_3)_n(H_3O^+)\right] + (n-1)\,H_2O + CH_3NH_2$$

$$(3)\ \ \left[(CH_3NH_3)_{n-1}(PbI_3)_n(H_3O^+)\right] \underset{\Delta}{\rightleftharpoons} (n-1)\,CH_3NH_3PbI_3 + H_2O + HI + PbI_2$$

Therefore, based on the XRD results (**Fig. S19 and S20**) after aging process, both hydrates and PbI$_2$ appeared. We considered that the decomposition process of perovskite without Spiro-NPU under high humidity includes the above (1), (2) and (3) processes. In detail, for the aged devices without Spiro-NPU, the escaped gas (CH$_3$NH$_2$ and HI) can destroy the continuity and smoothness of Spiro-OMeTAD and the metal electrode.[53] Moreover, the loss of CH$_3$NH$_2$ and HI from the active layer may greatly reduce the proportion of recovery extent. On contrast, even after a long-term aging process, the XRD of perovskite with Spiro-NPU only showed hydrate peaks, thus indicating that the (3) process of the decomposition reaction did not happen, possibly attributed by the protection of **Spiro-NPU** which blocks the volatilization of methylamine gas and facilitates the reverse reaction, as displayed in **Fig. S21**.

Simultaneously, the stability of perovskite devices with **Spiro-NPU** IEL against moisture and heat has also been investigated without any external encapsulations. The device structure is FTO/SnO$_2$/CH$_3$NH$_3$PbI$_3$/Spiro-NPU/Spiro-OMeTAD /Au, and the PCE was monitored at open circuit voltage. That after the exposure at 60% RH (room temperature in air) over 3000 h, nearly 100% of the initial *PCE* was remained (**Fig. 3e**). And at 85°C (55% RH in air) or 85% RH (25°C in air) over 500 h, the *PCE* still retained over 90% (**Fig. 3f, g**). On account that the surfaces of the devices are slightly wet at 85% RH, the PCE of the aged devices were measured after 1 min of thermal annealing at 100°C. To compare, the aged device without thermal post treatment maintained 70% of the original PCE (**Fig. 3g**). By contrast, the reference device without **Spiro-NPU** only preserved 42% of the initial efficiency after 7 days of aging, and recovered up to 55% PCE after same thermal process. Therefore, it is concluded that the **Spiro-NPU** can assist the

the original efficiency of same PSCs. The corresponding champion PCEs are 22.87%, 21.01% and 19.41% for PSCs original, PSCs-recovered and aged PSCs-recovered, respectively. We have also tested the stabilized power output (SPO) of the fresh and recovered devices over 20 minutes, as shown in **Fig. S23**, where the recovered device showed the same operational stability as the fresh device.

Meanwhile, the device with **Spiro-NPU** maintained 97% of their initial PCE after operating at the maximum power point (MPP) under 1 sun illumination (~50°C in the glovebox) for 200 hours (**Fig. 3h**), demonstrating superior operational stability. Therefore, we conclude that the **Spiro-NPU** IEL prominently enhances the moisture and thermal stability of PSCs.

While regarding to the fact that hydrophilicity of the additives in the Spiro-OMeTAD, such as lithium bis(trifluorome-thanesulfonyl)imide (Li-TFSI) and tertbutylpyridine (tBP), affects the long-term stability of perovskite,[55] the migration of dopants
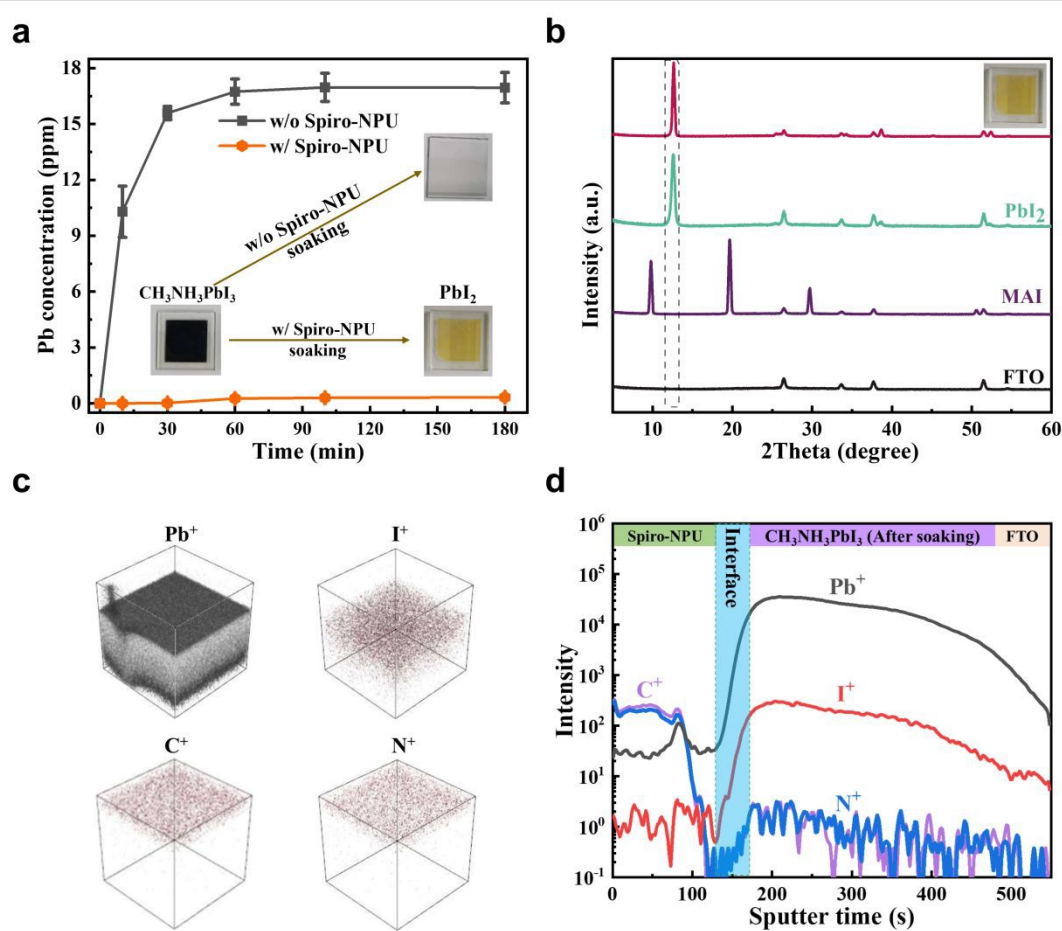

Fig. 4. Pb leakage. (**a**) Water-soaking test results for the CH$_3$NH$_3$PbI$_3$ w/o and w/ the IEL Pb-leaking measurement. The error bars represent the standard deviations from five samples for each condition. (**b**) XRD patterns of the soaked CH$_3$NH$_3$PbI$_3$/**Spiro-NPU**. (**c**) Spatial distribution of Pb$^+$, I$^+$, C$^+$, N$^+$ in FTO/perovskite/**Spiro-NPU**. (**d**) Depth profiles of the CH$_3$NH$_3$PbI$_3$ with **Spiro-NPU**.

recovery of the devitalized PSCs.

We further explored the stability of the PSCs-recovered with **Spiro-NPU**, as shown in the **Fig. S22**, at ambient atmosphere (60% RH @25°C) over 30 days. The aged PSCs-recovered maintains ~ 91% of their initial PCE, namely ~83% of

was also assessed. Li-TFSI and 4-tBP were deposited on top of FTO/**Spiro-NPU**, followed by the exposure at 85% RH (25 ^{o}C) over 500 hours, and we carried out the in-depth XPS analysis (Ar$^+$, 1 keV) on this aged film with etching time of 0 s, 120 s, 240 s, 360 s, 480 s and 600 s, respectively. As shown in **Fig. S24a and**

b, over 600s, the etching has not fully etched **Spiro-NPU**, thus the appearance of Li-TFSI and 4-tBP in **Fig. S24 c** and **d** reveals that the migration of dopants into **Spiro-NPU** is limited, which also explains the long-term stability of the IEL protected devices.

Lead Leakage

The Lead blocking capability of **Spiro-NPU** IEL was then studied by soaking the $CH_3NH_3PbI_3$ films (film size: 1.5 cm × 1.5 cm × 520 nm) directly in 10 mL deionized water, while the Pb concentration in water was detected via flame atomic absorption spectrophotometry (FAAS).[32] From **Fig. 4a**, in the first hour, the concentration of Pb rapidly increased and reached a platform of 17 ppm for pristine perovskite film, whereas barely Pb was found dissolved in water when it is covered with **Spiro-NPU** IEL. Further elongating the soaking time of perovskite wrapped with **Spiro-NPU** IEL to 3h, it is surprised to observe a yellow film, instead of a colorless one as it is for bare perovskite. According to the XRD (**Fig. 4b**), the left yellow film is the production of pure PbI_2, which explains the phenomenon that no Pb^{2+} was detected in the aqueous solution. Meanwhile, the $FTO/CH_3NH_3PbI_3$/Spiro-OMeTAD device was also soaked in water over 30 minutes. As observed in **Fig. S25,** PbI_2 was completely dissolved in water, leading to the contamination totally.

To understand this extraordinary property, the above decomposed yellow PbI_2/**Spiro-NPU** film was probed by time-of-flight secondary-ion mass spectrometry (TOF-SIMS),[56-58] which can detect the depth distribution of ions. And the depth profiles of Pb^+, I^+, C^+, N^+ are displayed in **Fig. 4c, d**, where the distributions of C^+, N^+ are coming from **Spiro-NPU** and Pb^+, I^+ are attributed to PbI_2. It is noted that nearly no Pb^+, I^+ were detected at the near top surface of **Spiro-NPU** IEL, while at the PbI_2/**Spiro-NPU** interface, their concentration gradually increased and reached to the platform at the PbI_2 layer. Thus, the **Spiro-NPU** IEL trapped almost all the Pb^{2+} in a short-term due to the Pb-O interaction as indicated in the XPS and ^1H NMR results (**Fig. 2g, 2h**), realizing a prominent lead blockage. To confirm this claim, we have extended the soaking time in water and tracked Pb^{2+} concentration (**Fig. S26**). In the first 20 days, the Pb concentration was limited at a very low level, less than 1 ppm, which was followed by a slowly increasing in the following 30 days to *ca*. 8 ppm on average. Further leaving the almost fully disappeared device in water, the Pb concentration remained constant (~8 ppm on average and 10 ppm maximum), demonstrating the final steady state of the Pb leakage. And this value is still comparatively lower than the Pb concentration of control device (~17 ppm) soaked in 1 hour. Therefore, even in the long-term soaking, **Spiro-NPU** can still effectively block lead leakage.

Spiro-PPU

On account of the above discussed properties and influence of **Spiro-NPU** IEL, the structure of internal encapsulating material has been adjusted, including the type of diisocyanate and the

selection of alkoxy chain. For instances, **Spiro-PPU** has also been synthesized by changing NDI block to 1,4-Phenylene-diisocyanate (PPDI) (**Scheme S1**). After a detailed similar investigation, it shows the same optical, electrical properties and the excellent performances as **Spiro-NPU** (Supplementary). Thereof, we are confident that our designed IEL is an efficient and multifunctional internal encapsulating material for devices based on organic-inorganic hybrid perovskites.

Conclusion

In summary, a multifunctional internal encapsulation material based on the *in-situ* co-polymerized, cross-linkable **Spiro-NPU** was obtained for perovskite solar cells. With its compatibility with Spiro-OMeTAD and high hole mobility, **Spiro-NPU** imparts the solar cells a high efficiency, *ca* 23.26% on rigid and 20.37% on flexible substrates. More importantly, the insertion of **Spiro-NPU** IEL yields remarkable enhancement of the moisture and thermal stability of perovskite films and devices. The perovskite film protected with **Spiro-NPU** IEL shows amazing water resistance of over 15 min, retained nearly 100% of PCE after aging in air (60% RH, 25 °C) for more than 3000 h. Moreover, the long-term aged photovoltaic-inactive hydrated phase of perovskite films could be converted back into photovoltaic-active black phase after annealing (or one solar irradiation), the PSCs have also demonstrated a promising repairability. Finally, based on the interaction of Pb-O with the perovskite and **Spiro-NPU** IEL, the lead leakage from the perovskite films has been eliminated yielding an excellent, and highly desired environmental effect. Therefore, we believe that internal encapsulation is an effective and promising way to finally solve the stability problem of perovskite solar cells, as well as other devices based on organic-inorganic perovskite materials, especially with the synergetic effect of a proper EEL.

Author contributions

Dongdong Xu and Yue Jiang conducted the idea. Dongdong Xu synthesized target molecule and performed the electro-optical characterizations and the experiments on solar cells. Runsheng Mai designed the synthesis method. Cong Chen, Ru Wang, Zhengjie Xu coordinated the research activity. Krzysztof Kempa, Guofu Zhou and Jun-Ming Liu contributed to the revision of the manuscript. The manuscript was written by Dongdong Xu, Yue Jiang and Jinwei Gao. Yue Jiang and Jinwei Gao directed the work. All the authors approved the final version of the manuscript.

Competing interests

The authors declare no competing interests.

References

Journal Name

1   NREL, "Best Research-Cell Efficiency Chart | Photovoltaic Research| NREL," https://www.nrel.gov/pv/cell-efficiency.html.

2   J.-P. Correa-Baena, M. Saliba, T. Buonassisi, M. Grätzel, A. Abate, W. Tress and A. Hagfeldt, Science, 2017, 358, 739.

3   L. K. Ono, Y. Qi and S. Liu, Joule, 2018, 2, 1961-1990.

4   Z. Fu, M. Xu, Y. Sheng, Z. Yan, J. Meng, C. Tong, D. Li, Z. Wan, Y. Ming, A. Mei, Y. Hu, Y. Rong and H. Han, Adv. Funct. Mater., 2019, 29, 1809129.

5   M. Bonomo, B. Taheri, L. Bonandini, S. Castro-Hermosa, T. M. Brown, M. Zanetti, A. Menozzi, C. Barolo and F. Brunetti, ACS Appl. Mater. Interfaces, 2020, 12, 54862-54875.

6   M. Wong-Stringer, O. S. Game, J. A. Smith, T. J. Routledge, B. A. Alqurashy, B. G. Freestone, A. J. Parnell, N. Vaenas, V. Kumar, M. O. A. Alawad, A. Iraqi, C. Rodenburg and D. G. Lidzey, Adv. Energy Mater., 2018, 8, 1801234.

7   L. Shi, M. P. Bucknall, T. L. Young, M. Zhang, L. Hu, J. Bing, D. S. Lee, J. Kim, T. Wu, N. Takamure, D. R. McKenzie, S. Huang, M. A. Green and A. W. Y. Ho-Baillie, Science, 2020, 368, eaba2412.

8   R. Cheacharoen, C. C. Boyd, G. F. Burkhard, T. Leijtens, J. A. Raiford, K. A. Bush, S. F. Bent and M. D. McGehee, Sustainable Energy & Fuels, 2018, 2, 2398-2406.

9   R. Cheacharoen, N. Rolston, D. Harwood, K. A. Bush, R. H. Dauskardt and M. D. McGehee, Energy Environ. Sci., 2018, 11, 144-150.

10 S. Ma, Y. Bai, H. Wang, H. Zai, J. Wu, L. Li, S. Xiang, N. Liu, L. Liu, C. Zhu, G. Liu, X. Niu, H. Chen, H. Zhou, Y. Li and Q. Chen, Adv. Energy Mater., 2020, 10, 1902472.

11 D. J. Slotcavage, H. I. Karunadasa and M. D. McGehee, ACS Energy Lett., 2016, 1, 1199-1205.

12 W. Xiang, S. Liu and W. Tress, Energy Environ. Sci., 2021, 14, 2090-2113.

13 H. Zhang, Z. Chen, M. Qin, Z. Ren, K. Liu, J. Huang, D. Shen, Z. Wu, Y. Zhang, J. Hao, C.-s. Lee, X. Lu, Z. Zheng, W. Yu and G. Li, Adv. Mater., 2021, 33, 2008487.

14 H. Lee and C. Lee, Adv. Energy Mater., 2018, 8, 1702197.

15 E. Bi, H. Chen, F. Xie, Y. Wu, W. Chen, Y. Su, A. Islam, M. Grätzel, X. Yang and L. Han, Nat. Commun., 2017, 8, 15330.

16 Z. Li, L. Wang, R. Liu, Y. Fan, H. Meng, Z. Shao, G. Cui and S. Pang, Adv. Energy Mater., 2019, 9, 1902142.

17 D. W. Ferdani, S. R. Pering, D. Ghosh, P. Kubiak, A. B. Walker, S. E. Lewis, A. L. Johnson, P. J. Baker, M. S. Islam and P. J. Cameron, Energy Environ. Sci., 2019, 12, 2264-2272.

18 X. Meng, Z. Xing, X. Hu, Z. Huang, T. Hu, L. Tan, F. Li and Y. Chen, Angew. Chem. Int. Ed., 2020, 59, 16602-16608.

19 Y. Zhao, J. Wei, H. Li, Y. Yan, W. Zhou, D. Yu and Q. Zhao, Nat. Commun., 2016, 7, 10228.

20 D. Bi, C. Yi, J. Luo, J.-D. Décoppet, F. Zhang, Shaik M. Zakeeruddin, X. Li, A. Hagfeldt and M. Grätzel, Nat. Energy, 2016, 1, 16142.

21 Z. Huang, X. Hu, C. Liu, L. Tan and Y. Chen, Adv. Funct. Mater., 2017, 27, 1703061.

22 Q. Cao, Y. Li, H. Zhang, J. Yang, J. Han, T. Xu, S. Wang, Z. Wang, B. Gao, J. Zhao, X. Li, X. Ma, S. M. Zakeeruddin, W. E. I. Sha, X. Li and M. Grätzel, Sci. Adv., 2021, 7, eabg0633.

23 F. Li, J. Yuan, X. Ling, Y. Zhang, Y. Yang, S. H. Cheung, C. H. Y. Ho, X. Gao and W. Ma, Adv. Funct. Mater., 2018, 28, 1706377.

24 F. Tan, H. Tan, M. I. Saidaminov, M. Wei, M. Liu, A. Mei, P. Li, B. Zhang, C.-S. Tan, X. Gong, Y. Zhao, A. R. Kirmani, Z. Huang, J. Z. Fan, R. Quintero-Bermudez, J. Kim, Y. Zhao, O. Voznyy, Y. Gao, F. Zhang, L. J. Richter, Z.-H. Lu, W. Zhang and E. H. Sargent, Adv. Mater., 2019, 31, 1807435.

25 Q. Wang, Q. Dong, T. Li, A. Gruverman and J. Huang, Adv. Mater., 2016, 28, 6734-6739.

26 M. Kim, S. G. Motti, R. Sorrentino and A. Petrozza, Energy Environ. Sci., 2018, 11, 2609-2619.

27 J. Peng, J. I. Khan, W. Liu, E. Ugur, T. Duong, Y. Wu, H. Shen, K. Wang, H. Dang, E. Aydin, X. Yang, Y. Wan, K. J. Weber, K. R. Catchpole, F. Laquai, S. De Wolf and T. P. White, Adv. Energy Mater., 2018, 8, 1801208.

28 H. Zhang, J. Shi, L. Zhu, Y. Luo, D. Li, H. Wu and Q. Meng, Nano Energy, 2018, 43, 383-392.

29 Z. Dai, S. K. Yadavalli, M. Chen, A. Abbaspourtamijani, Y. Qi and N. P. Padture, Science, 2021, 372, 618-622.

30 S. Wu, Z. Li, M.-Q. Li, Y. Diao, F. Lin, T. Liu, J. Zhang, P. Tieu, W. Gao, F. Qi, X. Pan, Z. Xu, Z. Zhu and A. K. Y. Jen, Nat. Nanotechnol., 2020, 15, 934-940.

31 S. Chen, Y. Deng, X. Xiao, S. Xu, P. N. Rudd and J. Huang, Nature Sustainability, 2021, 4, 636-643.

32 X. Li, F. Zhang, H. He, J. J. Berry, K. Zhu and T. Xu, Nature, 2020, 578, 555-558.

33 Y. Jiang, L. Qiu, E. J. Juarez-Perez, L. K. Ono, Z. Hu, Z. Liu, Z. Wu, L. Meng, Q. Wang and Y. Qi, Nat. Energy, 2019, 4, 585-593.

34 S. Chen, Y. Deng, H. Gu, S. Xu, S. Wang, Z. Yu, V. Blum and J. Huang, Nat. Energy, 2020, 5, 1003-1011.

35 J. Hári and B. Pukánszky, in Applied Plastics Engineering Handbook, ed. M. Kutz, William Andrew Publishing, Oxford, 2011, DOI: https://doi.org/10.1016/B978-1-4377-3514-7.10008-X, pp. 109-142.

36 C. Check, B. Imre, H. Gojzewski, R. Chartoff and G. J. Vancso, Poly. Chem., 2018, 9, 1983-1995.

37 C. Cai, J. Tang, Y. Zhang, W. Rao, D. Cao, W. Guo, L. Yu and J. Ding, Adv. Healthcare Mater., n/a, 2102654.

38 M.-H. Li, J.-Y. Shao, Y. Jiang, F.-Z. Qiu, S. Wang, J. Zhang, G. Han, J. Tang, F. Wang, Z. Wei, Y. Yi, Y.-W. Zhong and J.-S. Hu, Angew. Chem. Int. Ed., 2021, 60, 16388-16393.

39 H. Chen, T. Liu, P. Zhou, S. Li, J. Ren, H. He, J. Wang, N. Wang and S. Guo, Adv. Mater., 2020, 32, 1905661.

40 X. Wu, Y. Jiang, C. Chen, J. Guo, X. Kong, Y. Feng, S. Wu, X. Gao, X. Lu, Q. Wang, G. Zhou, Y. Chen, J.-M. Liu, K. Kempa and J. Gao, Adv. Funct. Mater., 2020, 30, 1908613.

41 Y. Cai, J. Cui, M. Chen, M. Zhang, Y. Han, F. Qian, H. Zhao, S. Yang, Z. Yang, H. Bian, T. Wang, K. Guo, M. Cai, S. Dai, Z. Liu and S. Liu, Adv. Funct. Mater., 2021, 31, 2005776.

42 G. Rajendra Kumar, A. Dennyson Savariraj, S. N. Karthick, S. Selvam, B. Balamuralitharan, H.-J. Kim, K. K. Viswanathan, M. Vijaykumar and K. Prabakar, Phys. Chem. Chem. Phys., 2016, 18, 7284-7292.

43 J.-H. Kim, Y. R. Kim, B. Park, S. Hong, I.-W. Hwang, J. Kim, S. Kwon, G. Kim, H. Kim and K. Lee, Small, 2021, 17, 2005608.

44 Y. Wang, Q. Liao, J. Chen, W. Huang, X. Zhuang, Y. Tang, B. Li, X. Yao, X. Feng, X. Zhang, M. Su, Z. He, T. J. Marks, A. Facchetti and X. Guo, J. Am. Chem. Soc., 2020, 142, 16632-16643.

45 L. Wang, H. Zhou, J. Hu, B. Huang, M. Sun, B. Dong, G. Zheng, Y. Huang, Y. Chen, L. Li, Z. Xu, N. Li, Z. Liu, Q. Chen, L.-D. Sun and C.-H. Yan, Science, 2019, 363, 265.

46 J. Chen, X. Zhao, S.-G. Kim and N.-G. Park, Adv. Mater., 2019, 31, 1902902.

47 T.-S. Su, F. T. Eickemeyer, M. A. Hope, F. Jahanbakhshi, M. Mladenović, J. Li, Z. Zhou, A. Mishra, J.-H. Yum, D. Ren, A. Krishna, O. Ouellette, T.-C. Wei, H. Zhou, H.-H. Huang, M. D. Mensi, K. Sivula, S. M. Zakeeruddin, J. V. Milić, A. Hagfeldt, U. Rothlisberger, L. Emsley, H. Zhang and M. Grätzel, J. Am. Chem. Soc., 2020, 142, 19980-19991.

48 C.-L. Mai, Q. Zhou, Q. Xiong, C.-C. Chen, J. Xu, Z. Zhang, H.-W. Lee, C.-Y. Yeh and P. Gao, Adv. Funct. Mater., 2021, 31, 2007762.

49 Y. Zhao, P. Zhu, S. Huang, S. Tan, M. Wang, R. Wang, J. Xue, T.-H. Han, S.-J. Lee, A. Zhang, T. Huang, P. Cheng, D. Meng, J.-W. Lee, J. Marian, J. Zhu and Y. Yang, J. Am. Chem. Soc., 2020, 142, 20071-20079.

50 W. Ke, C. C. Stoumpos, I. Spanopoulos, M. Chen, M. R. Wasielewski and M. G. Kanatzidis, ACS Energy Lett., 2018, 3, 1470-1476.

51 S. Chen, X. Xiao, B. Chen, L. L. Kelly, J. Zhao, Y. Lin, M. F. Toney and J. Huang, Sci. Adv., 2021, 7, eabb2412.

52 F. Hao, C. C. Stoumpos, Z. Liu, R. P. H. Chang and M. G. Kanatzidis, J. Am. Chem. Soc., 2014, 136, 16411-16419.

53 Y. Han, S. Meyer, Y. Dkhissi, K. Weber, J. M. Pringle, U. Bach, L. Spiccia and Y.-B. Cheng, *J. Mater. Chem. A*, 2015, **3**, 8139-8147.

54 A. M. A. Leguy, Y. Hu, M. Campoy-Quiles, M. I. Alonso, O. J. Weber, P. Azarhoosh, M. van Schilfgaarde, M. T. Weller, T. Bein, J. Nelson, P. Docampo and P. R. F. Barnes, Chem. Mater., 2015, 27, 3397-3407.

55 H. Zhu, Y. Ren, L. Pan, O. Ouellette, F. T. Eickemeyer, Y. Wu, X. Li, S. Wang, H. Liu, X. Dong, S. M. Zakeeruddin, Y. Liu, A. Hagfeldt and M. Grätzel, *J. Am. Chem. Soc.*, 2021, **143**, 3231-3237.

56 S.-G. Kim, T. H. Le, T. de Monfreid, F. Goubard, T.-T. Bui and N.-G. Park, Adv. Mater., 2021, 33, 2007431.

57 Y. Chen, X. Zuo, Y. He, F. Qian, S. Zuo, Y. Zhang, L. Liang, Z. Chen, K. Zhao, Z. Liu, J. Gou and S. Liu, Adv. Sci., 2021, 8, 2001466.

58 X. Li, S. Fu, W. Zhang, S. Ke, W. Song and J. Fang, Sci. Adv., 2020, 6, eabd1580.

Energy & Environmental Science Accepted Manuscript